metals

MDPI

Article

Influence of Copper Addition on the Mechanical Properties and Corrosion Resistance of Self-Hardening Secondary Aluminium Alloy AlZn10Si8Mg

Martin Mikolajčík [1,*], Lenka Kuchariková [1], Eva Tillová [1], Jon Mikel Sanchez [2], Zuzana Šurdová [1] and Mária Chalupová [1]

[1] Faculty of Mechanical Engineering, Department of Materials Engineering, University of Žilina, Univerzitna 8215/1, 010 26 Zilina, Slovakia; lenka.kucharikova@fstroj.uniza.sk (L.K.); eva.tillova@fstroj.uniza.sk (E.T.); zuzana.surdova@fstroj.uniza.sk (Z.Š.); maria.chalupova@fstroj.uniza.sk (M.C.)

[2] TECNALIA, Basque Research and Technology Alliance (BRTA), Astondo Bidea E-700, 48160 Derio, Spain; jonmikel.sanchez@tecnalia.com

* Correspondence: martin.mikolajcik@fstroj.uniza.sk

Abstract: Aluminium alloys have a wide range of applications, mainly due to their advantageous strength-to-weight ratio, denoted as specific strength and corrosion resistance. In recent decades, there has been a notable surge in the usage of recycled alloys, attributed to their reduced production costs and emissions. One of the conditions for secondary production is the optimal sorting of used scrap. Once the aluminium scrap has been melted, it is tough to reduce the content of the various additives. Copper is the primary alloying element in some aluminium alloys, which leads to an increased amount of copper in the aluminium scrap. Therefore, it is important to investigate its effect on the properties of aluminium alloys in which it is not commonly present. For this reason, this paper is concerned with the influence of copper on the microstructure and properties of the secondary aluminium alloy AlZn10Si8Mg. Specifically, it compares two melts of self-hardening AlZn10Si8Mg alloys differing in copper content (0.019% and 1.72%). A complex quantitative and metallographic analysis by optical and electron microscopy has been performed. Mechanical properties were investigated by tensile test, Brinell hardness, and Vickers microhardness measurements. The corrosion resistance of the individual melts was verified by the Audi test.

Keywords: recycled aluminium; secondary aluminium alloys; AlZn10Si8Mg; self-hardening alloys; effect of Cu; tensile; hardness; microhardness; corrosion resistance; Audi test

Citation: Mikolajčík, M.; Kuchariková, L.; Tillová, E.; Sanchez, J.M.; Šurdová, Z.; Chalupová, M. Influence of Copper Addition on the Mechanical Properties and Corrosion Resistance of Self-Hardening Secondary Aluminium Alloy AlZn10Si8Mg. *Metals* **2024**, *14*, 776. https://doi.org/10.3390/met14070776

Academic Editor: Frank Czerwinski

Received: 22 May 2024
Revised: 20 June 2024
Accepted: 27 June 2024
Published: 30 June 2024

1. Introduction

In recent decades, recycling has been increasingly used for aluminium production to protect the environment. This production methodology offers substantial benefits including reduced carbon dioxide emissions, significant energy savings, and conservation of the resources. Approximately 10 to 15 times less energy is required for secondary production. As bauxite is only found in a small number of countries in the world, the production of secondary alloys enables other countries to reduce at least part of their dependence on the supply of this resource. Western countries, particularly in the transport sector, have high aluminium recycling rates, exceeding 95%. Notably, a significant portion of recycled aluminium is used in producing Al-Si alloys, predominantly in the automotive industry. The proportion of secondary aluminium alloys is expected to increase [1,2].

Many different types of aluminium alloys are used, the chemical composition of which depends on the required properties. Alongside desired alloying elements, aluminium alloys invariably contain impurities, with Fe being the most prevalent in both primary and secondary alloys. It is a major problem, especially in recycled materials, because it is technologically difficult to remove so its content in the alloy gradually increases with

repeated recycling cycles. In aluminium casting alloys, it forms intermetallic phases such as Al_3Fe, Al_8Fe_2Si, β-Al_5FeSi, etc. The most detrimental of these are the β—Al_5FeSi phases. These large-sized particles have the shape of thin plates which are visible as needles in the metallographic plane. The Al_5FeSi phases have a weak bond with the matrix and act as stress concentrators. They adversely affect the mechanical properties, causing brittleness, reduced ductility, and castability. The negative effect of the presence of Fe on the fatigue properties of aluminium alloys is widely acknowledged [3–6].

The addition of Mn as an alloying element affects the morphology of ferrous phases, thereby reducing the negative impact of Fe. Under the influence of Mn, intermetallic phases in the shape of Chinese script, skeletons, or polyhedrons are formed instead of the harmful brittle plate-like Al_5FeSi phase. This change has a positive effect on both mechanical and fatigue properties. Structural refinement ensues with an optimally chosen Mn content, characterised by a reduction in the Secondary Dendrite Arm Spacing (SDAS). This phenomenon underscores the potential for Mn alloying to enhance the performance of aluminium alloys [3,7].

Cu is one of the most important alloying additives in aluminium alloys due to its high solubility and strengthening effect. Many commercial alloys contain Cu either as the main additive or as one of the main alloying elements. The presence of Cu notably enhances strength and hardness in both as-cast and heat-treated conditions by facilitating the formation of Al_2Cu precipitates. Typically, alloys aiming for optimal hardenability are alloyed with 4–6% Cu. To improve hardenability, Cu is often used in combination with Mg. However, Cu generally reduces resistance to general corrosion and, in specific compositions and material conditions, heightens susceptibility to stress corrosion. Cu additions also reduce resistance to hot tearing and reduce castability [3,7,8].

In addition to the chemical composition, other parameters also influence the properties. One of the most important factors is the presence of casting defects. The origin of casting defects can be different. In aluminium alloys, gas-induced pores and shrinkage are most found. Shrinkage cavities are defects that occur because of dimensional shrinkage during solidification, typically occurring in regions with inadequate melt volume. Gas-related defects are pores which are caused by the entrapment of air or gas mixtures within the material [9,10]. In conventional casting methods, gas porosity is most often caused by hydrogen. These hydrogen-induced pores are typically small and evenly distributed throughout the casting, arising from the rapid decrease in hydrogen solubility as temperature declines during solidification [9–11].

By comparing the mechanical properties of the primary and secondary aluminium alloy AlSi10MnMg(Fe), it was found that the presence of casting defects reduces the ductility of both alloys. The secondary alloy was more susceptible to pore formation due to its increased Fe content. For the samples in which the formation of casting defects was avoided, similar mechanical properties were measured as in the primary alloy [12].

The cooling rate is an important factor that affects the microstructure and, consequently, the properties of aluminium alloys. It depends on the type of mould, the thickness of the casting, or mould preheating. Rapid heat removal contributes to the formation of a fine-grained microstructure, which causes a significant improvement in mechanical properties, especially ductility, toughness, and hardness, but also corrosion resistance. It was found that the tensile strength of A356 alloy was improved with increasing cooling rate, due to the transformation of the Al5FeSi to Al18Fe2Mg7Si10 phases. The growth and coarsening time of the β-Al5FeSi plate-like phases was also shortened. The maximum UTS of 225.3 MPa was reached by this alloy at a cooling rate of 1.11 °C/s. On the contrary, employing too high cooling rate resulted in degraded mechanical properties due to localised subcooling. At a cooling rate of 1.95 °C/s, a UTS of only 212.59 MPa was achieved [13,14]. When casting A356 alloy into preheated moulds at different temperatures, a clear improvement in mechanical properties was found at higher cooling rates. This improvement stemmed from the refinement of α-phase dendrites due to a larger number of nucleation units. At the same time, the morphology of the eutectic Si changed, with Si gaining the form of short rods

or rounded grains in the microstructure at higher cooling rates. As the mould preheating temperature increased from 25 °C to 400 °C, the average width of eutectic silicon gradually increased from 3.4 µm to 4 µm. Average length of eutectic Si grew from 9.1 µm to 10.9 µm. The average grain size of α-Al increased from 507 µm to 571 µm [15].

Excellent corrosion resistance is one of the fundamental features of aluminium alloys, rendering them indispensable in industries such as automotive and aerospace, where resilience against atmospheric corrosion is crucial. Within the pH range of 4.0 to 8.5, aluminium demonstrates passivation, forming a protective layer of Al_2O_3 with a thickness spanning from 1 to 10 nm on its surface. This layer has high stability and prevents direct contact of the material with the environment, thus significantly slowing down corrosion processes. If the Al_2O_3 layer is mechanically or chemically damaged, cathodic and anodic reactions are immediately initiated to restore it. In more aggressive environments, particularly those containing acids, chlorides, or alkalis, dissolution of the passive Al_2O_3 layer can occur, leading to local corrosion. In the case of aluminium casting alloys, attack by pitting corrosion is most common. The pits enlarge over time and can cause damage to the material to a great depth. Failure of the protective layer generally occurs in areas with locally reduced corrosion resistance. These locations are most often various intermetallic phases. The problem is their different potentials. Most intermetallic phases behave cathodically regarding the aluminium matrix, leading to the formation of microgalvanic cells. In terms of corrosion resistance, the most undesirable intermetallic phase is Al_5FeSi, but Cu- and Zn-based phases can also have a negative effect [16–23].

Self-hardening aluminium alloys, such as AlZn10Si8Mg, represent a category of aluminium alloys distinguished by their optimal properties without the need for additional heat treatment. These materials age naturally at room temperature. The required precipitation period resulting in suitable mechanical and fatigue properties is 7–10 days. In the automotive industry, self-hardening alloys are gaining in popularity thanks to the possibility of avoiding the heat treatment process. In the automotive industry, they are mainly used to produce cyclically loaded components, displacing AlSi7Mg0.3 and AlSi7Mg0.6 alloys. Compared to these materials, self-hardening AlZn10Si8Mg alloys have higher fatigue resistance due to the more favourable morphology of the individual structural components, particularly the eutectic Si. Thus, they are mainly used in those components where superior fatigue resistance is required. For these reasons, the self-hardening alloy AlZn10Si8Mg emerges as a highly promising alternative [24–27].

Currently, two variants of the self-hardening alloy AlZn10Si8Mg are used in the industry. They differ significantly in Fe and Mn content (Table 1) [28]. In Unifont alloys, the Cu content is notably limited. The aim of this study is to verify whether it is possible to use an AlZn10Si8Mg alloy with a higher Cu content and to describe its influence on the mechanical properties and corrosion resistance. Unifont 94 alloy with higher Fe content is produced only by high-pressure die casting. Therefore, the aim is to investigate the influence of the casting method on the structure and properties of these higher Fe AlZn10Si8Mg secondary alloys.

Table 1. Chemical composition of Unifont alloys [29] and experimental material [wt.%].

Alloy	Zn	Si	Mg	Fe	Mn	Cu	Ti	Al
Unifont 90	9–10	8.5–9.5	0.3–0.5	0.15	0.10	0.03	0.15	ball.
Unifont 94	9–10	8.5–9.5	0.3–0.5	0.40	0.40	0.03	0.10	ball.
A	9.299	8.949	0.309	0.840	0.743	0.019	0.117	ball.
B	11.590	8.360	0.250	0.620	0.570	1.720	0.040	ball.

2. Materials and Methods

The experimental material was a self-hardening secondary aluminium alloy AlZn10Si8Mg with increased iron content. Due to the high iron content, manganese was introduced into both compared melts to avoid the negative effect of iron. The investigated alloys differ

significantly in copper and zinc content. Melt B has a higher percentage of these alloying elements. The complete chemical composition is given in Table 1.

Alloy A was cast by company UNEKO, Ltd., Zátor, Czech Republic. The alloy was provided in the form of round bars with a diameter of 20 mm and a length of 300 mm. Casting was conducted in sand moulds at temperatures ranging from 700 to 710 °C, followed by refinement using ECOSAL AL 113S salt (KVS EKODIVIZE a.s, Horní Benešov, Czechia) at temperatures ranging from 695 to 705 °C. This alloy naturally precipitates within 7–10 days after casting. Alloy B was cast at the pilot casting plant of the TECNALIA, Irun, Spain. It was made using only recycled aluminium post-consumer scrap supplied by a local recycler. The scrap was melted and slagged in an induction furnace at temperature up to 800 °C. Subsequently, after the aluminium melt was slagged and skimmed, the melt was transferred to an electric resistance furnace and the alloying elements were adjusted to achieve the target composition in Table 1. The melt was refined with Al-Ti-B and modified with Al-Sr at 620 °C. Finally, the melt was poured into a preheated permanent steel mould at 200 °C.

The castings were sampled with an ATM Brillant 240 (ATM Qness GmbH, Mammelzen, Germany) saw for metallographic and quantitative microstructural analysis. The samples were embedded in dentacryl using a Struers CitoPress-1 embedder (Struers S.A.S., Champigny sur Marne, France). Subsequently, they underwent grinding and polishing using a Struers TegraPol-15 automatic machine, following a dedicated procedure to prepare Al-Si alloys. The different steps of this process vary in duration, sandpaper type, and environment. Before microstructure observation, the samples were etched with 0.5% HF and Dix–Keller.

A NEOPHOT 32 optical microscope (Carl Zeiss, Jena, Germany) was used for metallographic analysis of the individual melts. The microstructure images were taken with a Nikon DS-FI 1 camera (Nikon, Tokyo, Japan) and NIS Elements 5.20 software. The aim of the metallographic analysis was to identify the basic phases present in the structure of each melt. The distribution of these phases and casting defects was also studied. The same equipment was used for quantitative analysis to measure the structural parameters. The SDAS factor (Secondary Dendrite Arm Spacing), the area fraction of eutectic silicon, the size and area fraction of different ferrous phases, and the size and area fraction of casting defects were evaluated. All characteristics were observed at a minimum of 20 sample spots to ensure comprehensive analysis and reliable data collection.

The microstructure was further observed and documented with a TESCAN VEGA LMU II scanning electron microscope (TESCAN VEGA, Kohoutovice, Czech Republic). For this purpose, samples of each melt were prepared by a standard procedure. In addition to etching with 0.5% HF, the samples were deeply etched with concentrated HCl, enabling the 3D morphology of the individual phases to be observed after the alpha phase was etched away.

Brinell hardness tests were performed according to ISO 6506-1 [30] using CV-3000LDB hardness tester (LFC PTE LTD, Batam, Indonesia). A 5 mm diameter hard-metal ball was pressed for 10 s under a load of 250 kp. The reported hardness values represent the average of five measurements gained from the specimen. All measurements were performed at room temperature. Vickers microhardness was measured according to ISO 6507-1 [31] with a Zwick/Roell ZHμ microhardness tester (ZwickRoell, Ulm, Germany). A load of 10 g was applied for 10 s, with five indentations made for each phase. The resulting value represents the average of these measurements, ensuring a robust and accurate microhardness evaluation. Two samples of each alloy were used for microstructure observation and hardness measurements.

The tensile strength test was carried out according to ISO 6892-1 [32] by Instron 5985 (Instron, Norwood, MA, USA). Test bars were made from the castings of the tested melts by chip machining. For each melt, 3 proportional test bars with a diameter of 8 mm and an initial measured length L_o of 40 mm were produced. The fracture surfaces after tensile tests were evaluated using a selective electron microscope.

The corrosion resistance of the tested alloys was evaluated by the Audi test, which is an immersion gravimetric corrosion resistance test known for its efficiency. Three cylindrical samples of each alloy with a diameter of 15 mm and a height of 15 mm were produced by chip machining. They were carefully cleaned with distilled water and ethanol, then dried and weighed with high precision. To prevent contamination, the samples were handled exclusively with gloves or tweezers. The samples were then immersed in a solution of 25.6 mL of 35% HCl, 7.5 g of NaCl and 0.375 l of distilled water. The temperature of the solution during the test was 20 ± 2 °C. After two hours, the samples were again cleaned with distilled water and ethanol, dried, and weighed. Corrosion resistance was determined based on the weight loss of the samples during the test. The resulting weight change represents the average of three samples of a single alloy.

3. Results

3.1. Metallographic and Quantitative Analysis

3.1.1. Microstructure

Metallographic analysis was used to identify the phases that form the microstructure of the studied alloys. Figures 1 and 2 show the structure of alloy A. The largest area fraction is formed by dendrites of the alpha phase, representing the substitution solid solution of zinc in aluminium, visible as bright spots (Figure 1b). Interdendritic spaces host a eutectic formation characterised by crystals of eutectic silicon and alpha phase, visible as dark areas (Figure 1b).

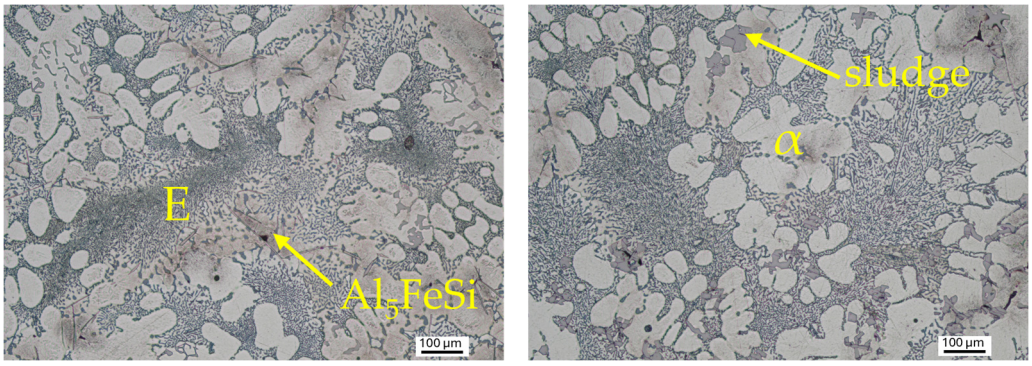

(**a**) (**b**)

Figure 1. Microstructure of alloy A, etch. Dix–Keller: (**a**) α-phase, eutectic, and Al_5FeSi needles; (**b**) α-phase, eutectic, and sludge phases.

Additionally, the structure of Alloy A comprises intermetallic phases. Plate/needle phases of Al_5FeSi (Figures 1a and 2c), skeletal phases of $Al_{15}FeMn_3Si_2$ (Figure 2a), and sludge phases based on Al-Fe-Mn (Figures 1b and 2c) are observed. The presence of manganese alloying contributes to the formation of sludge and skeletal iron phases within the structure. Furthermore, ternary eutectic Al-Mg_2Zn-Zn phases (Figure 2d) and Mg_2Si phases (Figure 2b,c) are identified, with Mg_2Si phases occasionally observed as dark skeletal units within the structure.

The microstructure of Alloy B, like Alloy A, is mostly composed of alpha-phase dendrites and eutectics in the interdendritic spaces (Figure 3a). However, in comparison to Alloy A, the structure of Alloy B is significantly finer. This difference can be attributed to the use of grain refiner and Sr modifier, as well as to the higher cooling rate due to the use of a metal mould. The structure contains needle/plate-like intermetallic Al_5Fesi phases (Figure 3b), skeleton-like $Al_{15}FeMn_3Si_2$ phases (Figure 3c), Al-Fe-Mn based sludge phases (Figure 3c,d). Skeletal Mg_2Si phases are occasionally observed within the microstructure.

The alloys differ visibly in the shape and size of the eutectic silicon. In Alloy A, the eutectic silicon crystals are shaped similarly to corals, growing as rods in clusters (Figure 4a).

In Alloy B, the eutectic silicon is significantly finer due to the use of the Sr modifier. The silicon grows around the intermetallic phases, but its shape is unrecognisable (Figure 4b).

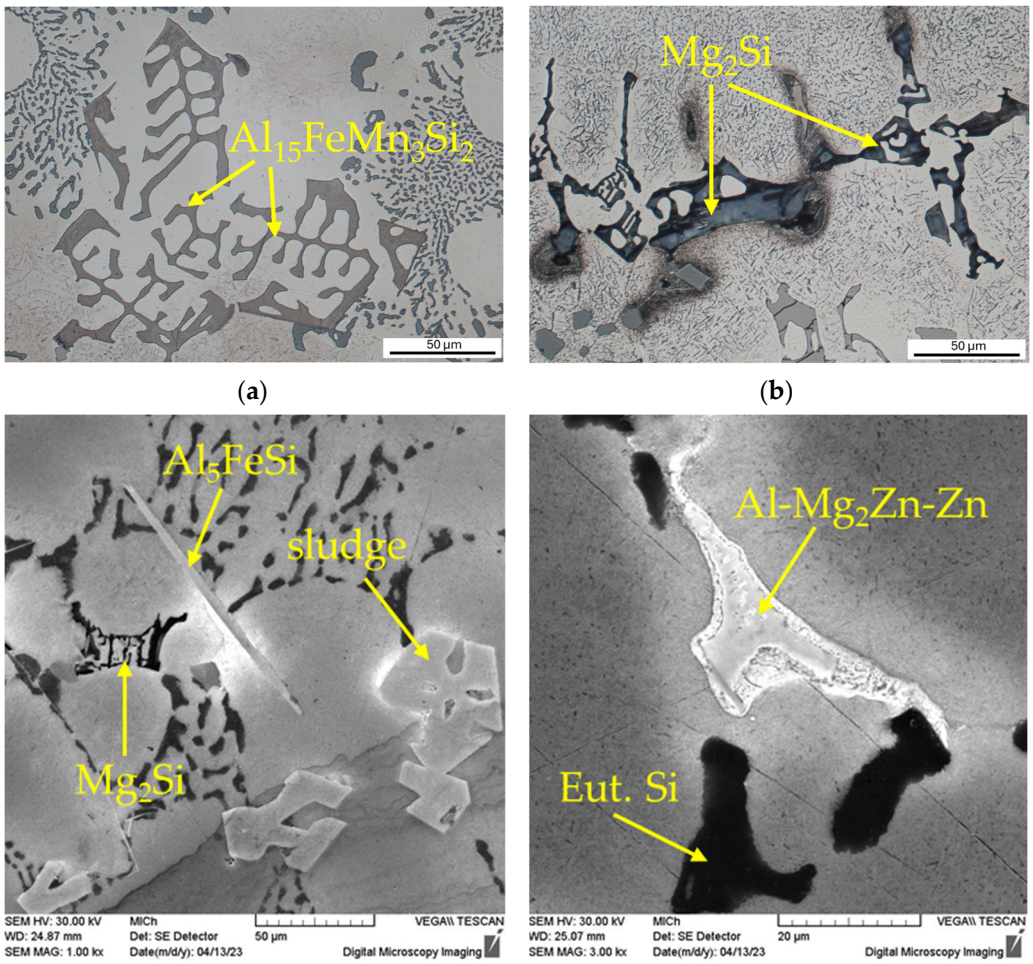

Figure 2. Details of the microstructure of alloy A: (**a**) skeleton-like $Al_{15}FeMn_3Si_2$ phases (etch. 0.5% HF); (**b**) skeleton-like Mg_2Si phases (etch. Dix–Keller); (**c**) sludge phases, Al_5FeSi needle, skeleton-like Mg_2Si phase (etch. 0.5% HF, SEM); (**d**) ternary eutectic Al-Mg_2Zn-Zn (etch. 0.5% HF, SEM).

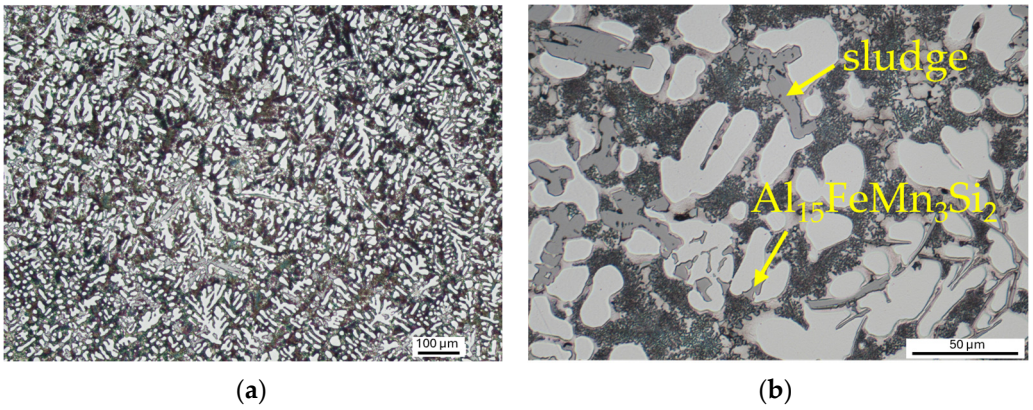

Figure 3. *Cont.*

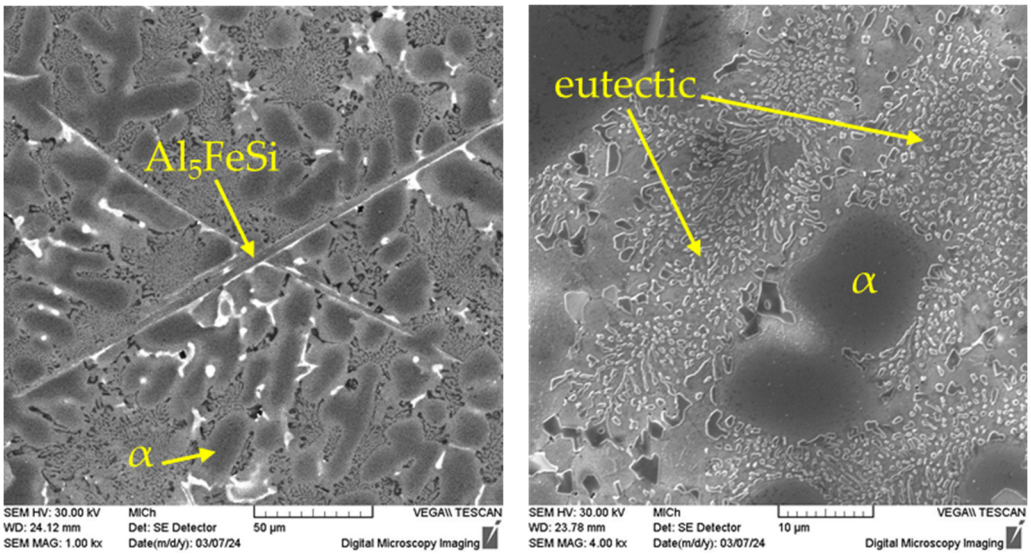

(**c**) (**d**)

Figure 3. Microstructure of alloy B: (**a**) alpha phase and eutectic, etch. Dix–Keller; (**b**) skeleton-like $Al_{15}FeMn_3Si_2$ phases and sludge Al-Fe-Mn phases, etch. Dix–Keller; (**c**) needle-like Al_5FeSi phases, etch. 0.5% HF, SEM; (**d**) detailed view of eutectic silicon crystals, etch. 0.5% HF, SEM.

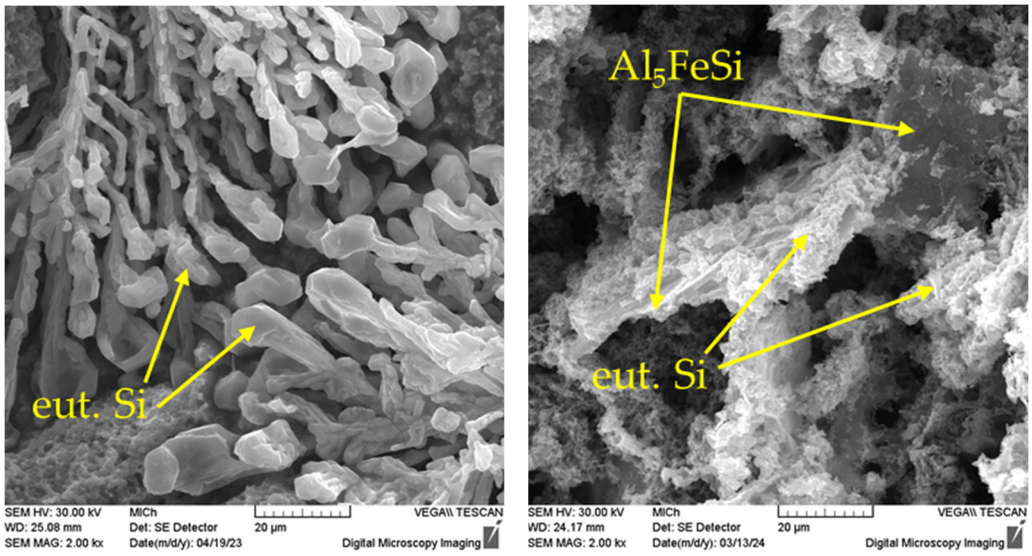

(**a**) (**b**)

Figure 4. Detailed view of eutectic silicon morphology, SEM, etch. HCl, deep etching: (**a**) alloy A; (**b**) alloy B, SEM.

Needle-like Al_5FeSi phases (Figure 5a) are generally undesirable in the microstructure of aluminium alloys. Their 3D morphology is plate-like, causing stress concentration in the material. Additionally, Al_5FeSi plates are very hard, and brittle compared to the matrix, resulting in the degradation of mechanical and fatigue properties. Due to the manganese alloying, the ferrous phases are found in the structure of the investigated alloys mainly in the form of skeleton (Figure 5c) and sludge phases (Figure 5b), which have a positive effect on the mechanical and fatigue properties. Skeleton-like Mg_2Si phases are occasionally observed within the microstructure.

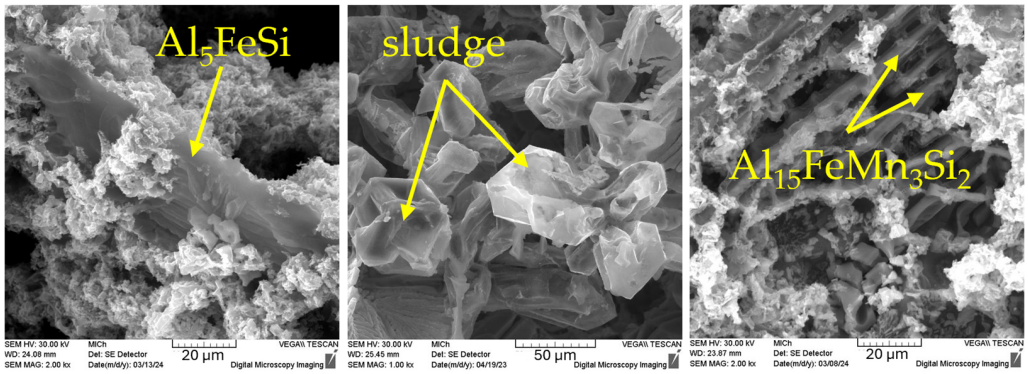

Figure 5. The 3D morphology of Fe-rich intermetallic phases, etch. HCl, deep etching: (**a**) plate-like Al_5FeSi phase; (**b**) Al-Fe-Mn sludge phases, SEM.

The identification of the various structural phases was also verified by EDX analysis using a scanning electron microscope. The presence of iron and manganese was proved in the sludge phases (Figure 6), which is in accordance with previous works of Sanchez [33], Liu [28], and Fu [34].

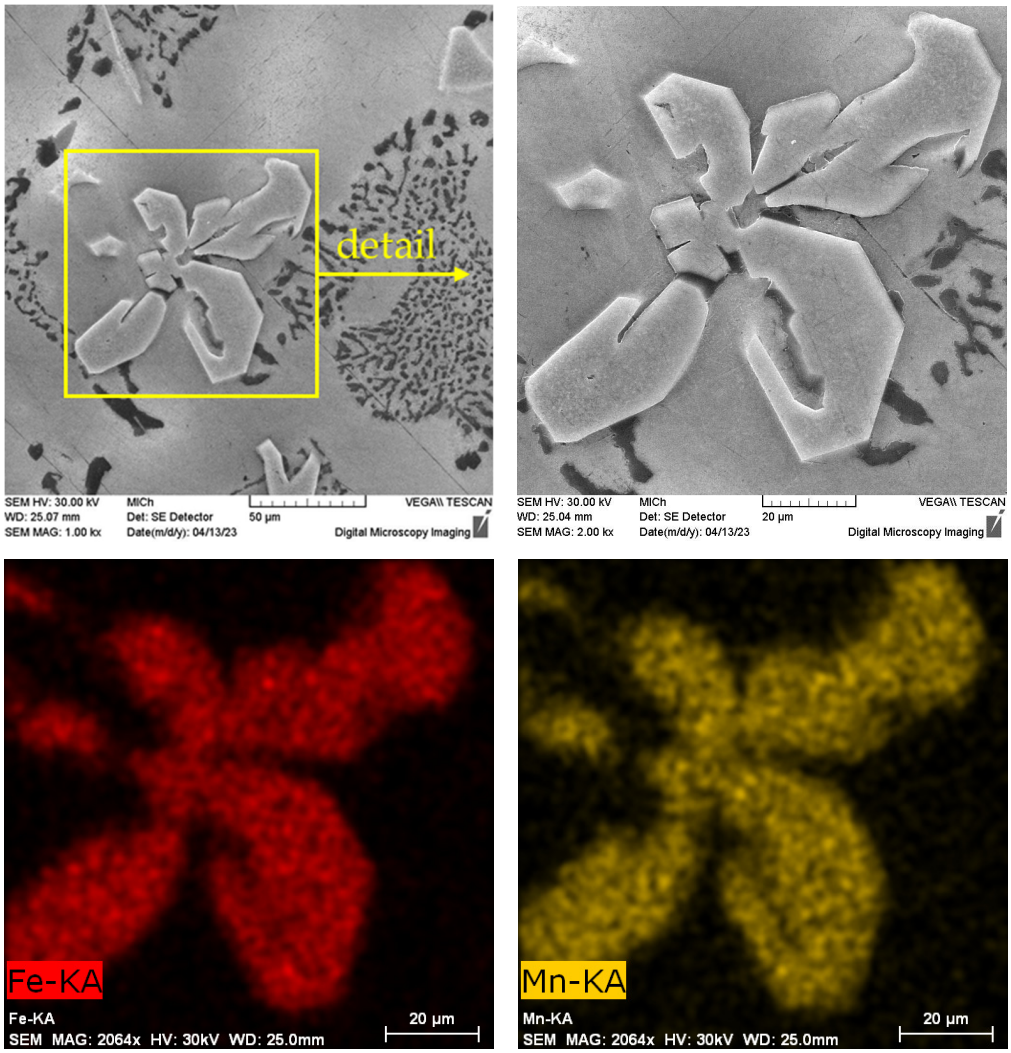

Figure 6. EDX analysis of sludge phase, etch. 0.5% HF, SEM.

3.1.2. Quantitative Analysis

By quantitative analysis, the structural parameters of the studied alloys were compared, providing deeper insight into the microstructure changes based on the chemical composition. The individual comparisons are presented in Figures 7–9. By comparing the area fraction of the individual phases, we found that their amount is significantly different in the tested alloys (Figure 7). Alloy B has a higher content of eutectic silicon, with up to a 5% increase compared to Alloy A. Sludge phases based on Al-Fe-Mn are the dominant intermetallic phases in both alloys. However, Alloy A has twice the amount of sludge phases (12.4%) compared to Alloy B. Due to the manganese alloying, needle-like phases occur only in small amounts in the microstructure of both alloys with a slightly higher area fraction observed in Alloy A. This alloy also has a significantly higher amount of casting defects.

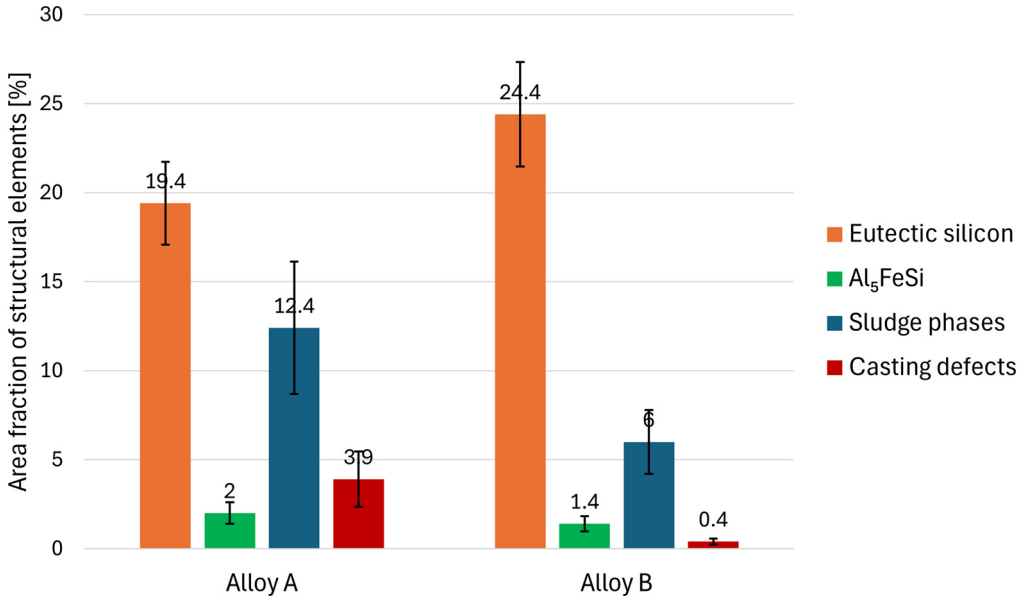

Figure 7. Results of quantitative analysis—area fraction of structural elements.

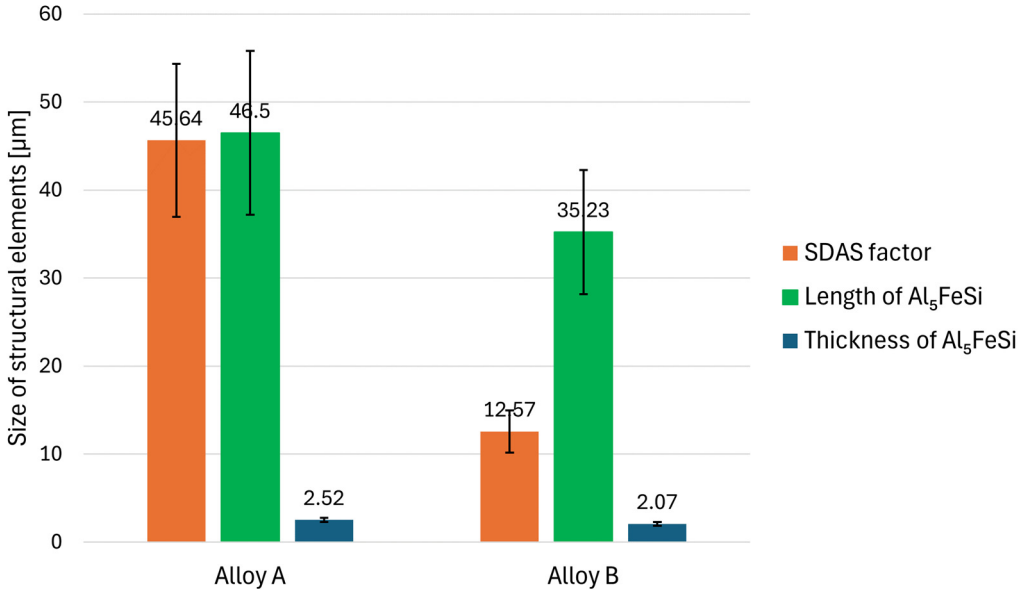

Figure 8. Results of quantitative analysis—size of Al_5FeSi and dendrites of α-phase.

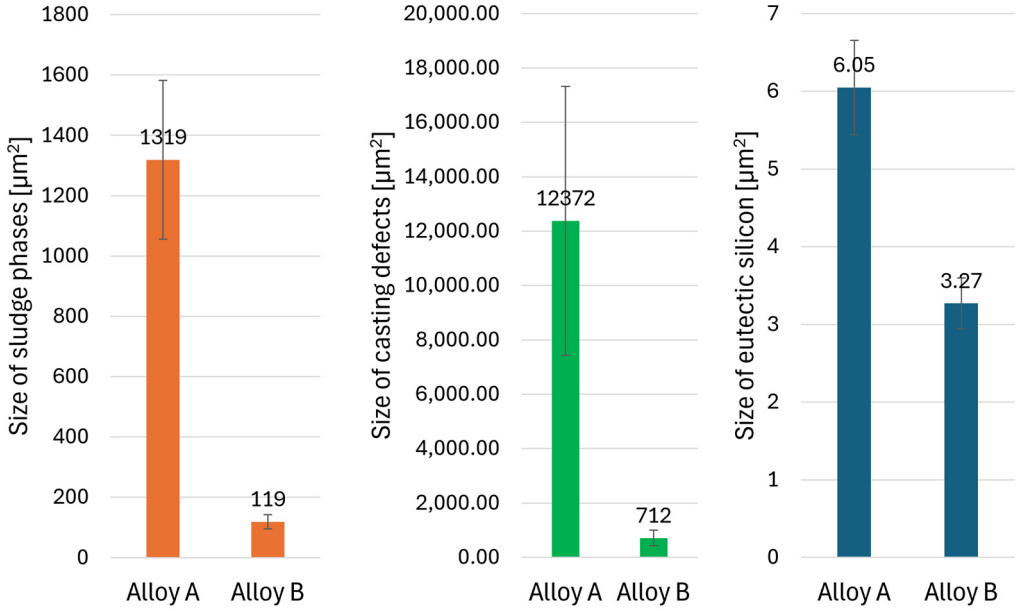

Figure 9. Results of quantitative analysis—size of structural elements.

The data presented in Figure 8 show that Alloy B has a significantly lower SDAS factor compared to Alloy A. This is likely attributed to the use of grain refiner and modifier in production combined with the higher cooling rate. The needle-like Al_5FeSi phases are longer and slightly thicker in Alloy A. Therefore, in combination with the reduced SDAS factor, an increase in mechanical properties, especially ductility, can be expected in Alloy B.

In addition to the higher area fraction of casting defects, the pores observed in Alloy A also have significantly larger dimensions. The casting defects in both alloys are mostly due to shrinkage during solidification, although gas pores are also present. Quantitative analysis confirmed that the eutectic silicon in Alloy B is notably finer, with smaller crystals, as previously identified in metallographic analysis (Figure 4). Conversely, in Alloy A, the ferrous sludge phases appear several times larger in size (Figure 9), contributing to the high area fraction of sludge phases in this alloy (Figure 7).

3.2. Mechanical Properties

The microstructure of aluminium alloys consists of many phases that differ significantly in their properties. When measuring hardness, it is important to consider that the measured hardness is strongly influenced by the microstructure directly at the point of indentation. Therefore, Brinell hardness measurement is recommended for cast aluminium alloys. The relatively large ball used in this measurement covers a larger area containing all structural phases, gaining more accurate results. Vickers microhardness HV0.01 was measured to detect differences in the hardness of each phase (Table 2). The hardest phases of the structure of AlZn10Si8Mg alloys are eutectic silicon and ferrous phases, while the dendrites of the alpha phase have the lowest hardness. The eutectic is composed of very hard crystals of eutectic silicon and soft alpha phase, resulting in higher hardness compared to the matrix. Sludge phases, being larger than needle phases, exhibit greater resistance when measuring hardness (Figure 10). In Alloy B, it is not possible to measure the hardness of the eutectic silicon because its crystals are too fine. The increased hardness of the alpha phase in Alloy B can be explained by the higher amount of eutectic in this alloy. The hard crystals of eutectic silicon are located just below the measured area, increasing the hardness of the matrix. The increased hardness of the eutectic is due to the tight arrangement of the smaller eutectic silicon crystals in Alloy B.

Table 2. Microhardness of individual phases (HV 0.01).

Alloy	α-Phase	Eutectic	Eut. Silicon	Sludge Phases	Al_5FeSi
A	101 ± 22	167 ± 35	1184 ± 151	1204 ± 146	588 ± 170
B	121 ± 31	191 ± 28	-	1355 ± 91	512 ± 36

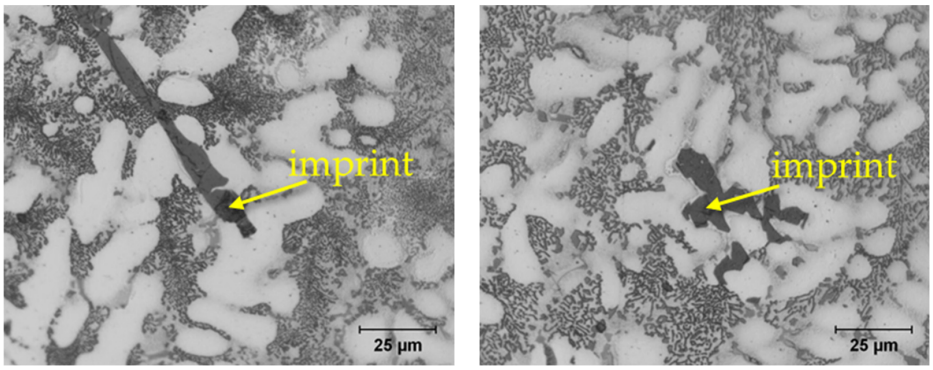

(**a**) (**b**)

Figure 10. Representative microhardness measurements of: (**a**) Al_5FeSi phase; (**b**) sludge phase.

By measuring the Brinell HBW 5/250/10 hardness, we found that Alloy B is significantly harder (Figure 11). This is probably due to the lower area fraction and size of casting defects leading to higher material resistance. Alloy B also has significantly higher Ultimate Tensile Strength (UTS) and Yield Tensile Strength (YTS). The UTS of Alloy B is almost double and the YTS is up to 145% that of Alloy A. Alloy B also has significantly higher UTS and YTS. The UTS of Alloy B is almost double and the YTS is up to 145% than that of Alloy A. These results, along with their respective tolerances, are summarised in Table 3.

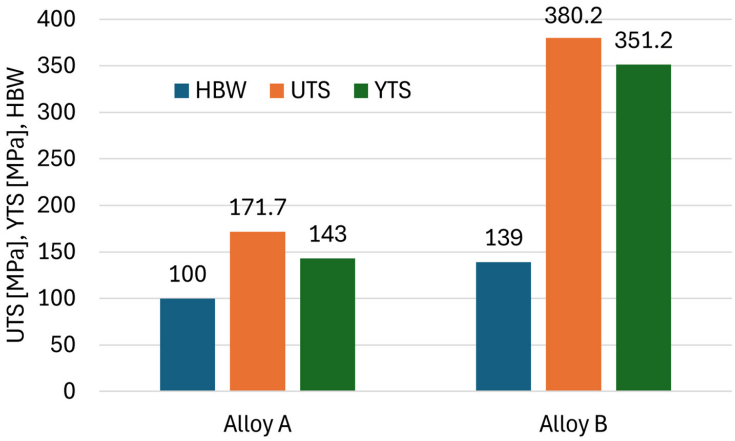

Figure 11. Brinell hardness, UTS, and YTS of investigated alloys.

Table 3. Overview of mechanical properties.

Alloy	UTS [MPa]	YTS [MPa]	Ductility [%]	HBW 5/250/10
A	171.7 ± 11	143 ± 37	0	100 ± 3
B	380.2 ± 8	351.2 ± 14	0.47	139 ± 3

The fracture surfaces of the test specimens were analysed with a selective electron microscope. Since the structure of AlZn10Si8Mg alloys is heterogeneous, a combination of ductile and cleavage failure is visible on the fracture surface (Figure 12a,b). Notably, porosity is visible on the fracture surface, with Alloy A exhibiting more extensive porosity. Consequently, the fracture surface of Alloy A appears more segmented. The failure occurred

in several planes because the strength of the material was locally reduced due to the influence of the pores.

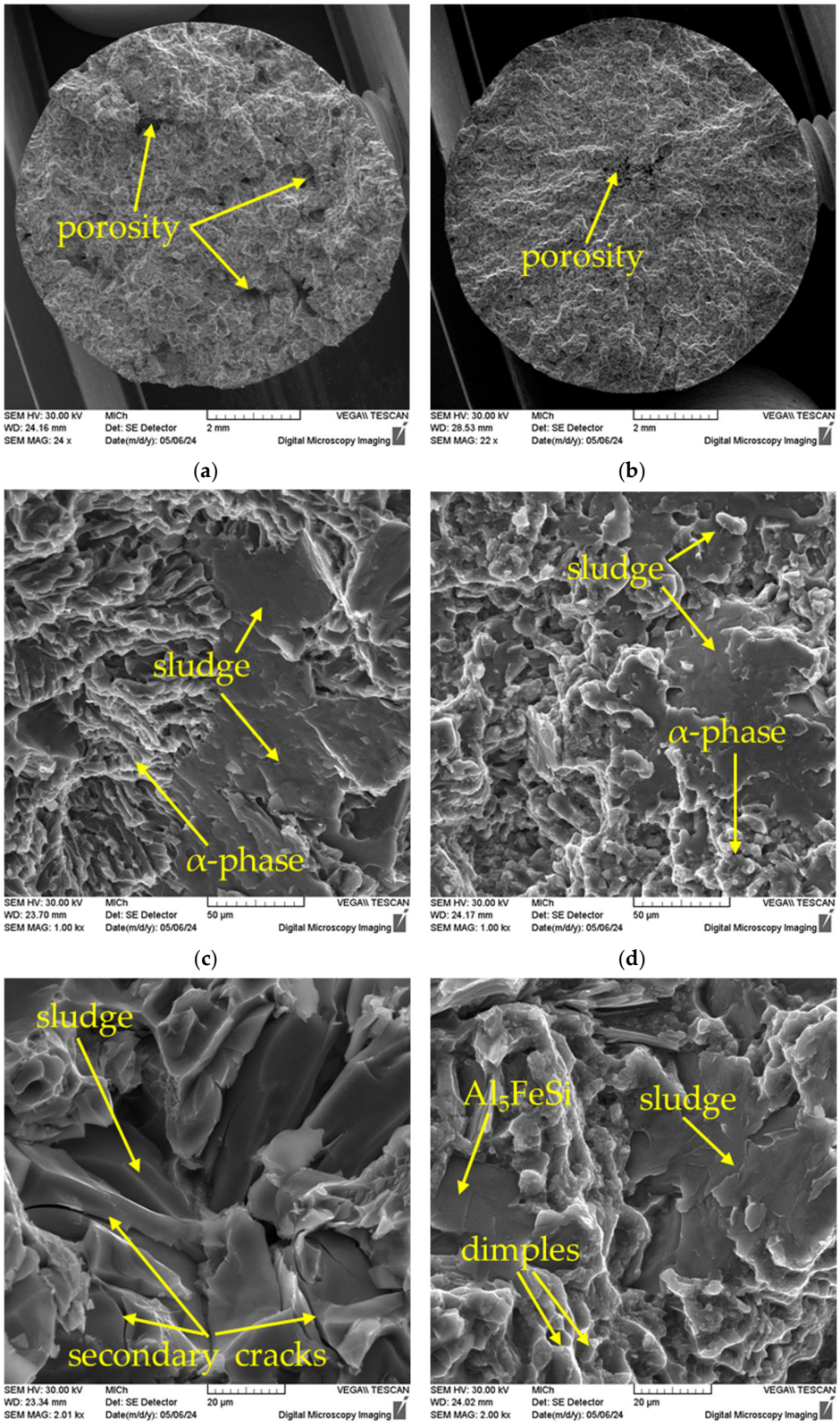

(**a**) (**b**) (**c**) (**d**) (**e**) (**f**)

Figure 12. Fractographic analysis of fracture surfaces, SEM: (**a**) overall view of A alloy sample; (**b**) overall view of B alloy sample; (**c**) detailed view of alloy A; (**d**) detailed view of alloy B; (**e**) cracking of sludge phase in Alloy A; (**f**) cleavage of ferrous phases and dimple morphology of the alpha phase.

The aluminium matrix in both alloys is fractured by transcrystalline ductile fracture with dimpled morphology. The size and shape of the dimples is defined by the size and shape of the eutectic silicon particles. The ferrous phases are ruptured predominantly by transcrystalline cleavage fracture (Figure 12c,d,f). In some cases, secondary fractures occur (Figure 12e). These different failure mechanisms arise from the different hardness of the different structural phases (Table 2). In Alloy A, sporadic occurrences of ferrous phases on the fracture surface are observed, which have not cleaved but instead separated at the interfacial boundaries (Figure 12e).

3.3. Corrosion Resistance

The corrosion resistance of the studied alloys was evaluated by measuring the weight loss following the Audi test (Figure 13). A lower weight loss indicates better corrosion resistance. The results revealed that Alloy B samples exhibited a weight loss of 0.582 ± 0.02 g, whereas Alloy A samples exhibited a weight loss of 0.792 ± 0.05 g during the test. These findings indicate that Alloy B demonstrates greater resistance to corrosion in this environment. However, the Audi test is not sufficient to characterise the corrosion resistance, so further research with more accurate methods is needed.

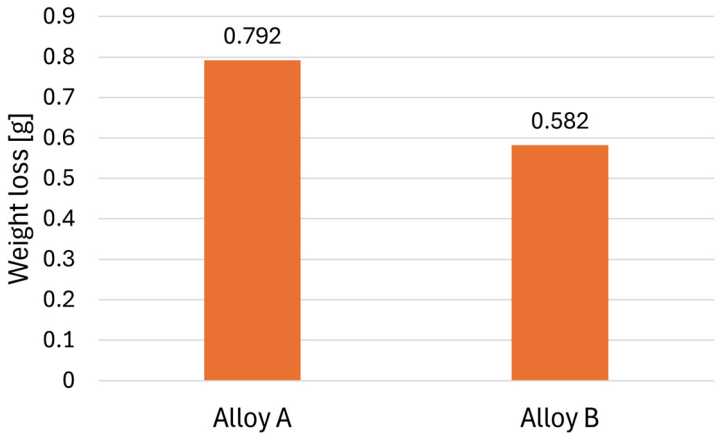

Figure 13. Results of the Audi test.

The weighing results were further validated by examining of the sample surfaces after the Audi test (Figure 14). Alloy A samples exhibit a greater extent of corrosion (Figure 14a). Upon closer inspection at higher magnification, general corrosion of the entire surface is observed. However, the surface of the specimen is attacked irregularly (Figure 14c). Corrosion initiation occurs where the protective oxide layer has been disrupted, particularly in the eutectic region, while the alpha-phase dendrites show better corrosion resistance. Irregular general corrosion is also visible on the surface of Alloy B (Figure 14b,d). Compared to Alloy A, there are fewer initiation points in this alloy with a damaged protective layer. The corrosion attack is less extensive and there is no significant penetration into the material.

By comparing the cross-sections of the samples of the investigated alloys after the Audi test, it was found that the corrosion attacked Alloy A to a significantly greater depth (Figure 15c,d). The finer microstructure of Alloy B played a significant role. Sludge iron phases cause eutectic dissolution because they form micro galvanic cells of two phases with different potentials (Figure 15e–h). Al_5FeSi needles have a stronger negative effect than sludge phases, as the latter possess potentials closer to the eutectic. While alpha-phase dendrites exhibit the highest resistance, they are also subjected to corrosion to a limited extent (Figure 15e). The influence of the individual phases on the corrosion mechanism did not change in the alloys studied. The enhanced corrosion resistance of Alloy B with a higher copper content may be attributed to the use of a grain refiner and modifier, which contributed to the fine microstructure.

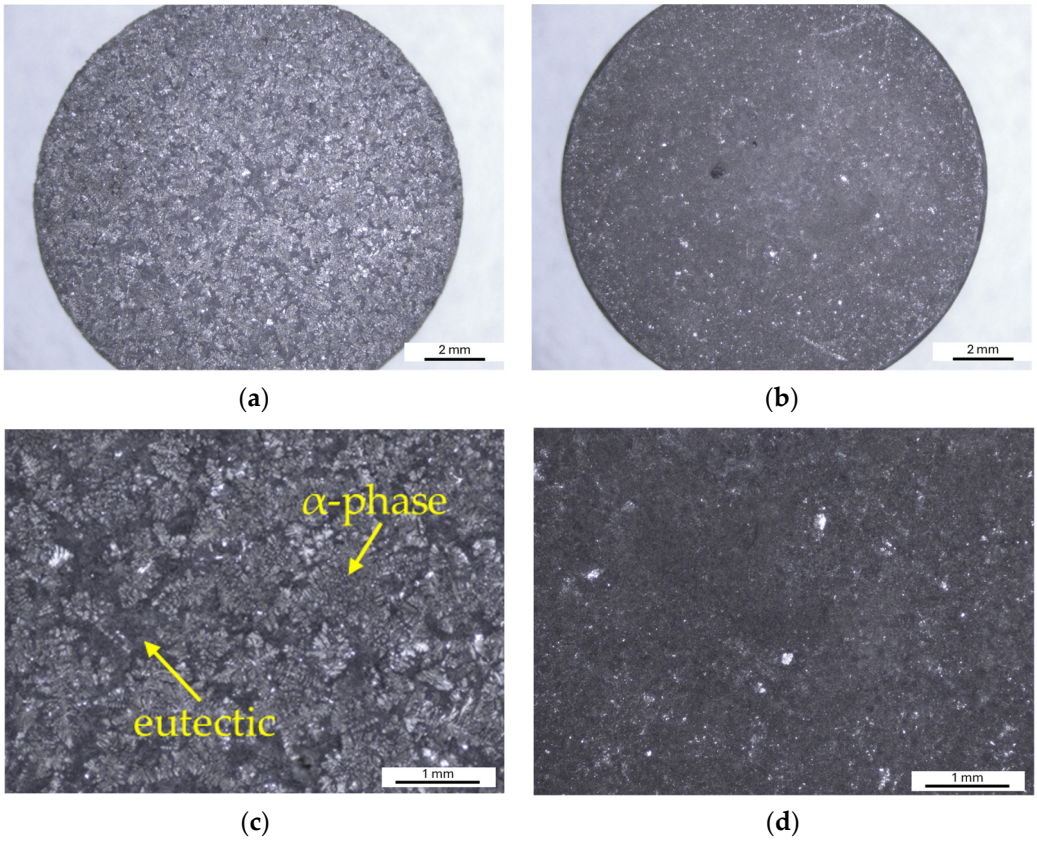

Figure 14. Surface of samples after the Audi test: (**a**) Alloy A; (**b**) Alloy B; (**c**) detail of Alloy A; (**d**) detail of Alloy B.

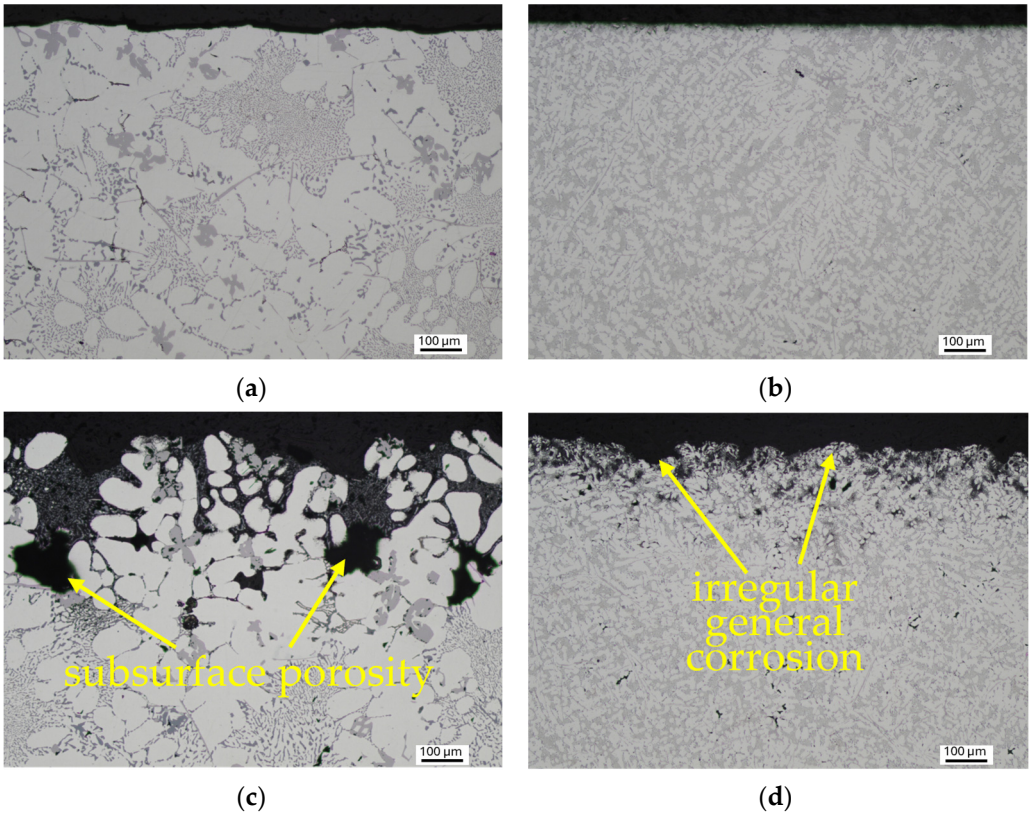

Figure 15. *Cont.*

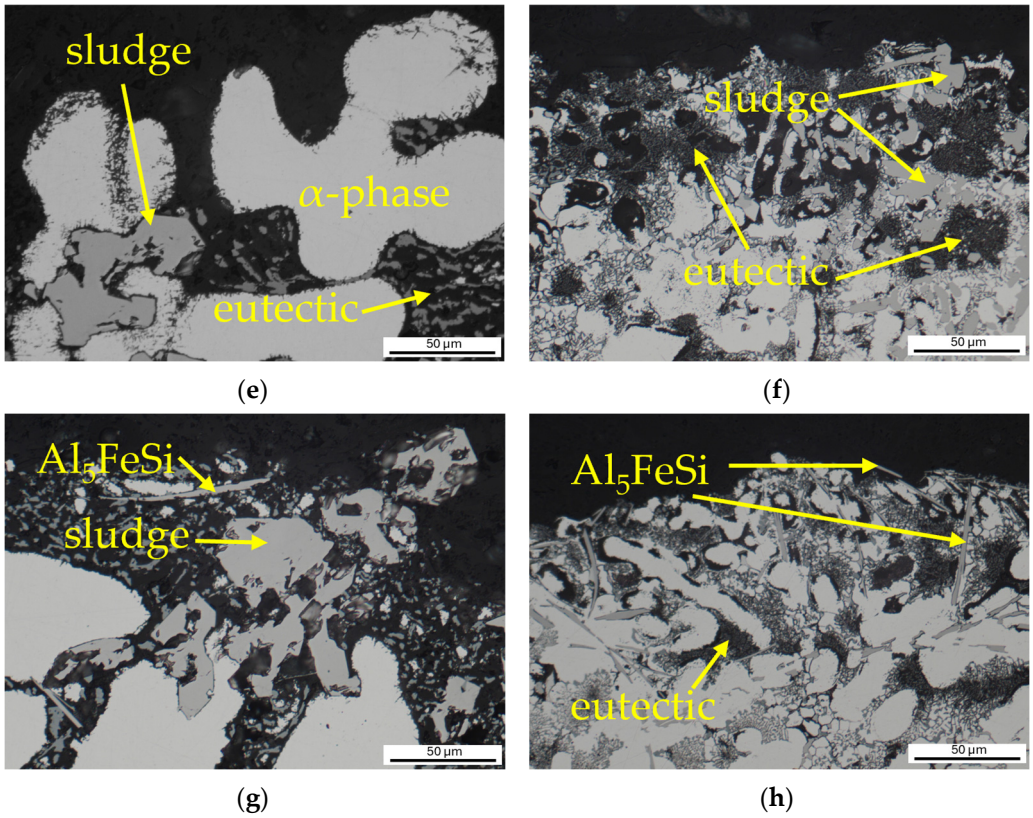

Figure 15. Documentation of the depth and mechanism of corrosion attack: (**a**) surface of the Alloy A without corrosion; (**b**) surface of the Alloy B without corrosion; (**c**) irregular general corrosion in Alloy A; (**d**) irregular general corrosion in Alloy B; (**e**) corrosion attack of eutectic in Alloy A; (**f**) corrosion attack of eutectic in Alloy B; (**g**) corrosion around intermetallic phases in Alloy A; (**h**) corrosion around Al_5FeSi in Alloy B.

4. Discussion

The results of our study provide valuable insights into the microstructural characteristics, mechanical properties, and corrosion behaviour of self-hardening aluminium alloys with varying compositions. The initial hypothesis that higher copper content in Alloy B might lead to the potential deterioration of corrosion resistance was not supported by the findings. Instead, Alloy B exhibited superior corrosion resistance compared to Alloy A, contrary to our expectations. This contradicts the results reported by Zhang [35], who reports that the susceptibility to intergranular corrosion increases in an Al-Zn-Mg-(Cu) alloy as the copper content increases from 0 to 2.6 wt.%. It should be noted, however, that the Audi test is not a reliable method for a comprehensive characterisation of the corrosion properties of the tested aluminium alloys. This test only provides a quick comparison of the behaviour of materials in a very aggressive environment. Hydrochloric acid creates an acidic environment that dissolves the protective oxide layer on the entire surface. The formation of corrosion products and the high porosity of Alloy A, which increases the reaction surface area of the sample, have a large influence on the observed mass loss. The Audi test thus only serves as a basis for long-term corrosion tests in a real environment and is insufficient to draw reliable conclusions. This unexpected outcome underscores the complexity of alloy behaviour and highlights the need for further research, as corrosion resistance is not only influenced by chemical composition. Rosso [27] reports that a finer structure positively affects the corrosion resistance of the AlZn10Si8Mg alloy, aligning with our finding of significantly improved corrosion resistance in Alloy B. Our findings contradict the results described by Kuchariková et al. in a previous work [36], in which the susceptibility of the AlZn10Si8Mg alloy to local corrosion is described. However, their tests were carried out in less aggressive environments where susceptibility to local forms of

corrosion is very likely. This corrosion was caused by the galvanic link between the eutectic and aluminium matrix. This resulted in the eutectic dissolving.

The improved mechanical properties due to the addition of copper correspond with the result of Wang [37], who reports that in the 2Al2 alloy with increased manganese content, the addition of copper increased the hardness and tensile strength from 228.3 to 255.6 MPa. The increased mechanical properties are due not only to the copper content but also to the production conditions, particularly the higher cooling rate of Alloy B due to the use of a metal mould. This argument was confirmed by Rosso [26], stating that the higher solidification rate promotes the formation of a finer microstructure and the improvement of the mechanical properties of the AlZn10Si8Mg alloy. The slow cooling rate caused the formation of larger Mg_2Si phases.

Scampone [38] reports that increasing zinc concentration in the AlSi7Cu2 alloy increases the eutectic content and promotes the formation of ferrous phases negatively affecting the ductility of the alloy. On the other hand, zinc causes the self-hardening ability due to which the mechanical properties are enhanced. Increasing zinc content reduces the necessary natural precipitation time. The resulting mechanical properties are also better at higher zinc contents. The matrix is harder due to the presence of zinc in the solid solution and hardening precipitates. Thus, the findings of Scampone [38] agree with our results. In alloy B, with higher zinc content, we found a higher proportion of eutectic (Figure 7) and a significant decrease in ductility (Figure 11). The UTS and YTS of this alloy were significantly higher, and the matrix hardness was also increased compared to Alloy A (Table 3).

In the broader context, our study underscores the significance of optimising alloy composition and processing parameters to enhance corrosion resistance in aluminium alloys. The findings have implications for industries reliant on aluminium components, such as the automotive and aerospace sectors, where corrosion resistance is critical for long-term performance and durability.

A summary of the experimentally determined structural, mechanical, and corrosion properties of the investigated AlZn10Si8Mg alloys is presented in Table 4. The different microstructure parameters resulted in a significant increase in UTS, YTS, and HBW in Alloy B.

Table 4. Overview of the observed characteristics of the investigated experimental alloys.

	Alloy A	**Alloy B**
Area fraction of eutectic silicon [%]	19.4	24.4
Area fraction of Al_5FeSi [%]	2	1.4
Area fraction of sludge phases [%]	12.4	6
Area fraction of casting defects [%]	3.9	0.4
SDAS factor [µm]	45.64	12.57
Length of Al_5FeSi [µm]	46.5	35.23
Thickness of Al_5FeSi [µm]	2.52	2.07
Size of sludge phases [μm^2]	1319	119
Size of casting defects [μm^2]	12372	712
Size of eutectic silicon [μm^2]	6.05	3.27
HBW 5/250/10	100	139
UTS [MPa]	171.7	380.2
YTS [MPa]	143	351.2
Weight loss after Audi test [g]	0.792	0.582

5. Conclusions

The microstructure, mechanical properties, and corrosion resistance of two self-hardening AlZn10Si8Mg alloys were compared in this study. The alloys differed significantly in copper and zinc content and cooling rate. The following conclusions can be drawn from our findings:

- The microstructure of the AlZn10Si8Mg alloy consists of the alpha phase, eutectic, intermetallic phases Al_5FeSi, $Al_{15}FeMn_3Si_2$, sludge phases Al-Fe-Mn, Al-Mg_2Zn-Zn, and Mg_2Si phases. With higher Cu and Zn contents, but especially with a faster cooling rate, the structure becomes significantly finer, and the proportion and size of ferrous intermetallic phases and the porosity decrease. On the contrary, the fraction of eutectic increases and the crystals of eutectic silicon are significantly finer.
- The hardness of individual phases in the AlZn10Si8Mg alloy varies significantly. The eutectic silicon crystals (1184 HV0.01), the sludge phase (1204 HV0.01), and the Al_5FeSi phase (588 HV0.01) are the hardest. Due to the higher zinc content, the hardness of the alpha phase is higher in Alloy B compared to Alloy A.
- The higher alpha phase hardness and eutectic hardness in Alloy B were also reflected in the overall Brinell hardness. In addition, Alloy B has significantly higher UTS and YTS due to the combination of higher copper and zinc content and finer microstructure. Thus, more efficient natural precipitation occurred in Alloy B.
- Due to the high level of hardening, the ductility of Alloy B decreased significantly. This brittleness primarily resulted from the presence of large-sized ferrous particles within the alloy. Under tensile stress, the matrix of both alloys was ruptured by transcrystalline ductile fracture. The ferrous phases were fractured by cleavage or separated along the interfacial interface. There was a noticeable porosity at the fracture surfaces.
- Contrary to expectations, Alloy B with a higher content of Cu was more corrosion-resistant than Alloy A. This is due to the significantly finer structure of this alloy. The corrosion resulted in the dissolution of the eutectic, which formed galvanic cells with an alpha phase. However, corrosion resistance is a complex subject, and no reliable conclusions can be drawn from immersion tests alone. Extensive research is therefore needed in this area using more accurate methods.

The issue of the corrosion resistance of the self-hardening alloy AlZn10Si8Mg is complex and requires consideration of multiple factors. Therefore, further research in this area is important. Even though commercially utilised alloys Unifont 90 and Unifont 94 have a permissible copper content no higher than 0.03%, this study demonstrates that with appropriate manufacturing conditions, excellent mechanical properties can be achieved even with higher copper content. These results might be especially significant for producers of secondary aluminium alloys when the input raw materials have a high copper percentage.

Author Contributions: Conceptualization, M.M., E.T., and J.M.S.; methodology, M.M., E.T., and J.M.S.; software, M.M. and M.C.; validation, E.T. and J.M.S.; formal analysis, Z.Š.; investigation, M.M., E.T., and J.M.S.; resources, M.M. and Z.Š.; data curation, M.M.; writing—original draft preparation, M.M.; writing—review and editing, E.T. and Z.Š.; visualization, M.M.; supervision, E.T. and L.K.; project administration, E.T.; funding acquisition, E.T. and L.K. All authors have read and agreed to the published version of the manuscript.

Funding: The research was funded by following grants: VEGA 1/0461/24 Study of a new generation of secondary (recycled) Al-alloys, I-23-028-04 Effect of manganese on fatigue resistance of secondary AlZn10Si8Mg aluminium alloy, KEGA č. 009ŽU-4/2023 Internationalization of education of foreign students at FME UNIZA in material and technological study programs, and KEGA č. 004ŽU-4/2023 New methods of education and support of soft skills in engineering study at the Faculty of Mechanical Engineering, University of Žilina. Basque Government through the project Elkartek SosIAMet KK-2022/00110.

Data Availability Statement: The data presented in this study are available on request from the corresponding author. The data are not publicly available due to ongoing research into these alloys.

Conflicts of Interest: Author Jon Mikel Sanchez was employed by the company TECNALIA, Basque Research and Technology Alliance (BRTA). The remaining authors declare that the research was conducted in the absence of any commercial or financial relationships that could be construed as a potential conflict of interest.

References

1. Padamata, S.K.; Yasinskiy, A.; Polyakov, P. A Review of Secondary Aluminum Production and Its Byproducts. *JOM* **2021**, *73*, 2603–2614. [CrossRef]
2. Wallace, G. Production of secondary aluminium. In *Fundamentals of Aluminium Metallurgy*, 1st ed.; Lumley, R., Ed.; Woodhead Publishing Limited: Cambridge, UK, 2011; pp. 70–82. [CrossRef]
3. Panchal, H.; Singh, S.; Sharma, R.; Solanki, K.; Kahar, S. The effect of alloying additions on the structure and properties of Al-Mg-Zn-Si-Mn alloy: A review. *Int. J. Sci. Dev. Res. (IJSDR)* **2023**, *8*, 1256–1269.
4. Arrabal, R.; Mingo, B.; Pardo, A.; Mohedano, M.; Matykina, E.; Merino, M.C.; Rivas, A. Microstructure and corrosion behaviour of A356 aluminium alloy modified with Nd. *Mater. Corros.* **2015**, *66*, 535–541. [CrossRef]
5. Ji, S.; Yang, W.; Gao, F.; Watson, D.; Fan, Z. Effect of iron on the microstructure and mechanical property of Al-Mg-Si-Mn and Al-Mg-Si diecast alloys. *Mater. Sci. Eng. A* **2013**, *564*, 130–139. [CrossRef]
6. Huter, P.; Oberfrank, S.; Grun, F.; Stauder, B. Thermo-mechanical fatigue influence of copper and silicon on hypo-eutectic Al–Si–Cu and Al–Si–Mg cast alloys used in cylinder heads. *Int. J. Fatigue.* **2016**, *88*, 142–155. [CrossRef]
7. Shehadeh, L.M.; Jalham, I.S. The Effect of Adding Different Percentages of Manganese (Mn) and Copper (Cu) on the Mechanical Behavior of Aluminum. *Jordan J. Mech. Ind. Eng.* **2016**, *10*, 19–26.
8. Abdelaziz, M.H.; Samuel, A.M.; Doty, H.W.; Valtierra, S.; Samuel, F.H. Effect of additives on the microstructure and tensile properties of Al–Si alloys. *J. Mater. Res. Technol.* **2019**, *8*, 2255–2268. [CrossRef]
9. Fiorese, E.; Bonollo, F.; Timelli, G.; Arnberg, L.; Gariboldi, E. New classification of defects and imperfections for aluminum alloy castings. *Int. J. Met.* **2015**, *9*, 55–66. [CrossRef]
10. Kucharčík, L.; Bruna, M.; Sládek, A. Influence of Chemical Composition on Porosity in Aluminium Alloys. *Arch. Foundry Eng.* **2014**, *14*, 5–8. [CrossRef]
11. Samuel, A.M.; Samuel, E.; Songmene, V.; Samuel, F.H. A Review on Porosity Formation in Aluminum-Based Alloys. *Materials* **2023**, *16*, 2047. [CrossRef]
12. Niklas, A.; Bakedano, A.; Orden, S.; da Silva, M.; Nogués, E.; Fernandéz-Calvo, A.I. Effect of Microstructure and Casting Defects on the Mechanical Properties of Secondary AlSi10MnMg(Fe) Test Parts Manufactured by Vacuum Assisted high Pressure Die Casting Technology. *Mater. Today Proc.* **2015**, *2*, 4931–4938. [CrossRef]
13. Liu, Z.; Zhou, L.; Li, G. Effects of Cooling Rate on the Microstructure and Tensile Strength of A356 Alloy Wheels. In Proceedings of the 3rd International Conference on Material, Mechanical and Manufacturing Engineering, Guangzhou, China, 27–28 June 2015. [CrossRef]
14. Muthusamy, G.; Wagstaff, S.; Allanore, A. Effect of Cooling Rate During Solidification of Aluminum–Chromium Alloy. In *Light Metals 2020. The Minerals, Metals & Materials Series*; Springer: Cham, Switzerland, 2020. [CrossRef]
15. Alkathafi, M.H.; Khalil, A.A.; Abdalla, A.O. The Effect of Cooling Rate on the Microstructure of A356 Aluminium Alloy. *SVOA Mater. Sci. Technol.* **2020**, *2*, 91–100.
16. Kuchariková, L.; Pastierovičová, L.; Tillová, E.; Uhríčik, M.; Zatkalíková, V.; Šajgalík, M. The Influence of a Corrosive Environment on Fatigue and Mechanical Properties of An Al-Cast Alloy with Higher Fe Content. *Metals* **2023**, *13*, 1019. [CrossRef]
17. Kamarska, K. Investigation of the Corrosion Behaviour of Aluminium Alloy in Selected Environments. *Environ. Technol. Resour. Proc. Int. Sci. Pract. Conf.* **2019**, *3*, 92–94. [CrossRef]
18. Xhanari, K.; Finšgar, M.; Knez Hrnčič, M.; and Maver, U.; and Knez, Ž.; Seiti, B. Green corrosion inhibitors for aluminium and its alloys: A review. *RSC Adv.* **2017**, *7*, 27299–27330. [CrossRef]
19. Svobodová, J.; Luňák, M.; Lattner, M. Analysis of the Increased Iron Content on the Corrosion Resistance of the AlSi7Mg0.3 Alloy Casting. *Manuf. Technol.* **2019**, *19*, 1041–1046. [CrossRef]
20. Hanza, S.; Vrsalovič, L.; Štic, L.; Liveric, L. Corrosion investigations of Al-Si casting alloys in 0.6 M NaCl solution. *Eng. Rev.* **2020**, *41*, 115–123. [CrossRef]
21. Pastierovičová, L.; Kuchariková, L.; Tillová, E.; Chalupová, M.; Liptáková, T.; Švecová, I. Effect of different chloride environments on corrosion behavior of secondary AlSi7Mg0.6 cast alloy with higher Fe content. *Mater. Today Proc.* **2022**, *62*, 2450–2456. [CrossRef]
22. Peng, C.; Liu, Y.; Guo, M.; Gu, T.; Wang, C.; Wang, Z.; Sun, C. Corrosion and pitting behavior of pure aluminum 1060 exposed to Nansha Islands tropical marine atmosphere. *Trans. Nonferrous Met. Soc. China.* **2022**, *32*, 448–460. [CrossRef]
23. Kusmierczak, S.; Hren, I. Influence of AlSi7Mg0.3 Alloy Modification on Corrosion Behaviour in the Salt Environment. *Manuf. Technol.* **2019**, *19*, 802–806. [CrossRef]
24. Kuchariková, L.; Pastierovičová, L.; Tillová, E.; CHalupová, M.; Závodská, D. Investigation of Self-Hardening AlZn10Si8Mg Cast Alloy for the Automotive Industry. *Arch. Metall. Mater.* **2022**, *68*, 517–524. [CrossRef]
25. Rosso, M.; Peter, I.; Castella, C.; Molina, R. Properties of AlZn10Si8Mg Alloys for High Performances Application. *Light Metals 2014* **2016**, 213–218. [CrossRef]
26. Rosso, M.; Ildiko, P.; Castella, C.; Molina, R. Optimization of Composition for Self-hardening AlZn10Si8Mg Alloys. *Mater. Today Proc.* **2015**, *2*, 4949–4956. [CrossRef]
27. Peter, I.; Rosso, M.; Castella, C.; Molina, R. Self-Hardening Alloys for Automotive Application. *Mater. Sci. Forum.* **2014**, *794–796*, 1221–1226. [CrossRef]

28. Liu, T.; Karkkainen, M.; Natac, L.; Arvikar, V.; Levin, I.; Brever, L.N. Iron-rich intermetallics in high pressure die cast A383 aluminum alloys. *Intermetallics* **2020**, *126*, 106814. [CrossRef]
29. Rheinfelden Alloys. Primary Aluminium Casting Alloys. 2016. Available online: https://rheinfelden-alloys.eu/wp-content/uploads/2017/01/Leporello-Primary-Aluminium-Casting-Alloys_RHEINFELDEN-ALLOYS_2016_EN.pdf (accessed on 19 May 2024).
30. *ISO 6506-1*; Metallic Materials—Brinell Hardness Test. International Organization for Standardization: Geneva, Switzerland, 2014.
31. *ISO 6507-1*; Metallic Materials—Vickers Hardness Test. International Organization for Standardization: Geneva, Switzerland, 2018.
32. *ISO 6892-1*; Metallic Materials—Tensile Testing. International Organization for Standardization: Geneva, Switzerland, 2019.
33. Sanchez, J.M.; Arribas, M.; Galarraga, H.; de Cortazar, M.G.; Ellero, M.; Girot, F. Effects of Mn addition, cooling rate and holding temperature on the modification and purification of iron-rich compounds in AlSi10MnMg(Fe) alloy. *Heliyon* **2023**, *9*, e13005. [CrossRef] [PubMed]
34. Fu, Y.; Wang, G.G.; Hu, A.; Li, Y.; Thacker, K.B.; Weiler, J.P.; Hu, H. Formation, charakteristics and control of sludge in Al-containing magnesium alloys: An overview. *J. Magnes. Alloys* **2022**, *10*, 599–613. [CrossRef]
35. Zhang, M.; Liu, S.; Jiang, J.; Wei, W. Effect of Cu content on intergranular corrosion and exfoliation corrosion susceptibility of Al−Zn−Mg−(Cu) alloys. *Trans. Nonferrous Met. Soc. China* **2023**, *33*, 1963–1976. [CrossRef]
36. Kuchariková, L.; Liptáková, T.; Tillová, E.; Kajánek, D.; Schmidová, E. Role of Chemical Composition in Corrosion of Aluminum Alloys. *Metals* **2018**, *8*, 581. [CrossRef]
37. Wang, S.; Meng, G.; Song, M. Effect of Cu Addition on Properties of an Al-La Alloy. *Coatings* **2023**, *13*, 1505. [CrossRef]
38. Scampone, G.; Gursoy, O.; Brutti, S.; Timelli, G. Effect of Zn addition and natural aging on the microstructure and mechanical properties of secondary AlSi7Cu2 alloys. *IOP Conf. Ser. Mater. Sci. Eng.* **2023**, *1274*, 012057. [CrossRef]